



Determination of Electrode Oxygen Transport Kinetics Using Electrochemical Impedance Spectroscopy Combined with Three-Dimensional Microstructure Measurement: Application to $\text{Nd}_2\text{NiO}_{4+\delta}$

Kyle Yakal-Kremski,^{a,*} Liliana V. Moggi,^{b,c,**} Alejandra Montenegro-Hernández,^{b,c} Alberto Caneiro,^{b,c} and Scott A. Barnett^{a,**}

^aDepartment of Materials Science and Engineering, Northwestern University, Evanston, Illinois 60208, USA

^bConsejo Nacional de Investigaciones Científicas y Técnicas (CONICET), Ciudad Autónoma de Buenos Aires, Argentina

^cCaracterización de Materiales, Centro Atómico Bariloche, CNEA, CP 8400, S. C. de Bariloche, Argentina

Oxygen reduction kinetic parameters – oxygen ion diffusion D_δ , molar surface exchange rate \mathfrak{R}_O and surface exchange coefficient k – were determined for porous $\text{Nd}_2\text{NiO}_{4+\delta}$ solid oxide fuel cell cathodes as a function of temperature and oxygen partial pressure by analyzing electrochemical impedance spectroscopy data using the Adler-Lane-Steele model. Electrode microstructural data used in the model calculations were obtained by three-dimensional focused ion beam-scanning electron microscope tomography. Cathodes were fabricated using $\text{Nd}_2\text{NiO}_{4+\delta}$ powder derived from a sol-gel method and were tested as symmetrical cells with LSGM electrolytes. The oxygen surface exchange rate exhibited a power-law dependency with oxygen partial pressure, whereas the oxygen diffusivity values obtained varied only slightly. The present analysis suggests that the O-interstitial diffusion has a bulk transport path, whereas the surface exchange process involves dissociative adsorption on surface sites followed by O-incorporation. For $\text{Nd}_2\text{NiO}_{4+\delta}$ at 700°C and 0.2 atm oxygen pressure, $D_\delta = 5.6 \cdot 10^{-8} \text{ cm}^2 \text{ s}^{-1}$, $\mathfrak{R}_O = 2.5 \cdot 10^{-8} \text{ mol} \cdot \text{cm}^{-2} \text{ s}^{-1}$. The present D_δ and \mathfrak{R}_O values and their activation energies are slightly different to those previously reported for $\text{Nd}_2\text{NiO}_{4+\delta}$ using other measurement methodologies, and lower than typical state-of-the-art Co-rich perovskites. However, the average $k_\delta = 1.0 \cdot 10^{-5} \text{ cm} \cdot \text{s}^{-1}$ at 700°C is comparable to those of fast oxygen exchange rate perovskites.

© The Author(s) 2014. Published by ECS. This is an open access article distributed under the terms of the Creative Commons Attribution Non-Commercial No Derivatives 4.0 License (CC BY-NC-ND, <http://creativecommons.org/licenses/by-nc-nd/4.0/>), which permits non-commercial reuse, distribution, and reproduction in any medium, provided the original work is not changed in any way and is properly cited. For permission for commercial reuse, please email: oa@electrochem.org. [DOI: 10.1149/2.0521414jes] All rights reserved.

Manuscript submitted August 19, 2014; revised manuscript received September 29, 2014. Published October 8, 2014. This was Paper 723 presented at the Orlando, Florida, Meeting of the Society, May 11–15, 2014.

Measurement of oxygen transport kinetics of mixed ionic and electronic conducting (MIEC) oxides is important to select appropriate oxides and to understand their performance in solid oxide fuel cells (SOFCs) and related devices such as electrolyzers and oxygen membranes. The two methods typically employed to measure the oxygen transport coefficients, i.e., oxygen surface exchange coefficient k and bulk oxygen diffusivity D , have different advantages and disadvantages. Isotope exchange depth profiling,^{1–3} evaluating the O-isotope labeled surface exchange (k^*) rate and diffusion coefficients (D^*), is widely used and accepted, but it utilizes dense pellets or thin films that have substantially different microstructure than actual electrodes. Furthermore, it is often difficult to accurately separate k^* and D^* from fitting the depth profiles. Conductivity and curvature relaxation methods^{4–7} face similar challenges with fabrication of bulk pellets or thin films, and separating both coefficients unambiguously. Here, the response to an applied chemical potential gradient is measured, yielding the chemical diffusion coefficient (D_{chem}) and the chemical surface reaction coefficient (k_{chem}).

Adler, et al.^{8,9} recently demonstrated an alternate method with different characteristics. The method calculates the oxygen transport coefficients by using the Adler-Lane-Steele (ALS) model¹⁰ with inputs from electrochemical impedance spectroscopy data, taken over a range of temperatures and oxygen partial pressures, and electrode morphology data. An advantage of this technique is that the values obtained correspond to an actual electrode microstructure, versus a dense bulk pellet or thin film. Furthermore, since porous MIEC electrodes are usually co-limited by the surface and bulk processes, it should be possible to obtain both surface and bulk kinetic coefficients with good accuracy.

The present paper describes the application of this method using full three-dimensional microstructure information, including the

MIEC tortuosity factor that is needed to obtain accurate kinetic parameters from the ALS model expressions. This work is also the first case where this method has been applied to a MIEC electrode material where the predominant mobile oxygen species are interstitials: the Ruddlesden-Popper (R-P) phase rare earth nickelate $\text{Nd}_2\text{NiO}_{4+\delta}$ (NNO). The prior report focused on perovskite-phase (La,Sr) CoO_3 that conducts oxygen ions through oxygen site vacancies.⁹ The R-P nickelate materials have recently attracted considerable interest as SOFC oxygen electrode materials based on their fast oxygen transport kinetics and good stability over a wide range of oxygen partial pressures.^{11–14} These oxides also have the advantages of being cobalt-free^{15,16} and Sr-free, such that they do not suffer from Sr surface segregation.^{17–19} Chemical stability in low oxygen partial pressures²⁰ is thereby increased compared with oxygen vacant perovskites such as Co-rich perovskite²¹ since the oxygen ion carrier is not a vacancy that is part of the basic structure of the crystal.

The diffusion and surface exchange coefficients of $\text{Ln}_2\text{NiO}_{4+\delta}$ (Ln = La, Pr, and Nd) nickelates have been evaluated by oxygen isotopic exchange^{22,23} and conductivity relaxation.^{24–26} However, it is difficult to obtain dense single-phase nickelate samples for these measurements²² due to the high sintering temperatures (1350°C), which induce surface modification due to species segregation. The present measurements avoid these difficulties, providing data that are representative of the actual electrode – ensuring that the same phases, surface segregation (if present), and morphological effects such as surface curvature and faceting are present. Furthermore, there is a wide variation in the reported kinetic parameters. The present D and k values are compared with those obtained by other methods, providing input to select the best experimental conditions for a proper evaluation of these coefficients.

The Nickelates

Figure 1 shows the crystal structure of $\text{Nd}_2\text{NiO}_{4+\delta}$.²⁷ This is one of several $\text{Ln}_2\text{NiO}_{4+\delta}$ compounds belonging to the Ruddlesden-Popper

*Electrochemical Society Student Member.

**Electrochemical Society Active Member.

†E-mail: KyleYakalKremski2014@u.northwestern.edu

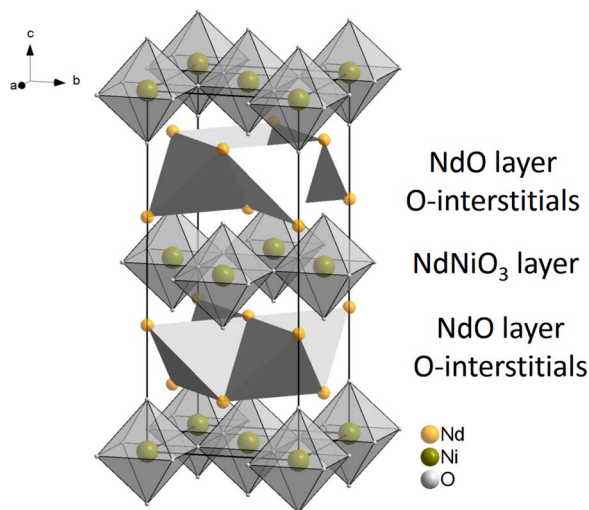


Figure 1. Crystal structure of $\text{Nd}_2\text{NiO}_{4+\delta}$. The O-interstitial sites are indicated with tetrahedrons coordinated with Nd atoms in the NdO layers.

phase ($\text{A}_{n+1}\text{B}_n\text{O}_{3n+1}$) with $n = 1$, the so called K_2NiF_4 -type or “nickelate” structures. The crystal structure consists of LnNiO_3 perovskite layers stacked alternating with rock salt LnO layers. The possibility to accommodate O-interstitials in the rock salt layer (tetrahedron sites) promotes oxygen hyperstoichiometry (δ); these oxygen interstitials can exhibit fast transport.²⁸ In addition to interstitials, oxygen transport can also occur via the migration of oxygen vacancies in the perovskite layers. However, the O-interstitial migration dominates the ionic conductivity due to the higher mobility of these defects.^{29,30} The ionic conductivity of the nickelates has been shown to be comparable to that of YSZ ,³¹ and superior to the O-vacancy conductivity in perovskite-like materials such as $\text{La}_{0.6}\text{Sr}_{0.4}\text{Fe}_{0.8}\text{Co}_{0.2}\text{O}_{3-\delta}$ (LSFC), and $\text{La}_{0.6}\text{Sr}_{0.4}\text{Fe}_{0.8}\text{Ni}_{0.2}\text{O}_{3-\delta}$ (LSFN).³²

The oxygen hyper-stoichiometry also induces Ni oxidation, generating electron-hole charge carriers³³ that contribute to p-type electronic conductivity. This, together with the oxygen ionic transport, guarantees the mixed conductivity of these materials. One unique characteristic of these material is that the interstitial concentration and ionic conductivity should remain high even under the highly oxidizing anodic potentials encountered in electrolysis; this is in contrast to the perovskites, where the vacancy concentration may decrease dramatically at high $p\text{O}_2$.³⁴ Thus, these materials are interesting as both SOFC cathode and solid oxide electrolyzer anode, and the determination of the kinetic parameters directly from electrochemical measurements in porous electrodes is fundamental to understand the mechanism of reaction and to design the best electrode microstructure.

Description of the Method

Generality of the ALS model.— Electrochemical impedance spectroscopy (EIS) measurements of MIEC oxide electrodes yield spectra that depend on oxygen transport, which includes both surface processes and diffusion.^{35,36} The ALS model was developed to describe the impedance response of porous single-phase MIEC oxides; although the model specifies a case where the ionic conductivity is dominated by O-vacancy species, the same basic framework can also be applied to interstitial nickelate materials, as described below. The ALS model leads to a specific electrical equivalent circuit – a Gerischer impedance element – with the form:

$$Z_G = R_G \frac{1}{\sqrt{j\omega\tau_G + 1}} \quad [1]$$

where Z_G is the complex impedance, $j = \sqrt{-1}$, R_G is the Gerischer resistance, and τ_G the Gerischer time constant given by:

$$R_G = \frac{RT}{4F^2} \frac{1}{\sqrt{4a\Re_O c_O x_\delta^0 D_{ef}}} \quad [2]$$

$$\tau_G = \frac{(1-\varepsilon)c_O x_\delta^0}{4a\Re_O A_O} \quad [3]$$

Note that R_G and τ_G depend on both material properties and electrode morphological features. \Re_O is the molar equilibrium oxygen surface exchange rate, D_{ef} is the effective defect diffusion coefficient, c_O is the concentration of oxygen sites involved in diffusion, x_δ^0 is the molar fraction of vacancy or interstitial defects at equilibrium, ε is the electrode porosity (such that $(1-\varepsilon)$ is the MIEC volume fraction), and a is the electrode specific surface area. Another morphological feature, the MIEC-phase tortuosity factor $\tau_s = \left(\frac{L_{eff}}{L}\right)^2$, which considers the ratio between the effective path length traveled by the diffusive specie to the straight distance, is contained within $D_{ef} = \frac{(1-\varepsilon)D_\delta}{\tau_s}$. The thermodynamic factor describing how the oxygen chemical potential μ_{O_2} varies with oxygen non-stoichiometry is given by

$$A_O = \pm \frac{1}{2RT} \frac{\partial \mu_{O_2}}{\partial \ln x_\delta} \quad [4]$$

where the (–) sign corresponds to O-vacancies and (+) to O-interstitials.

In order to obtain accurate kinetic parameters using the present method, the electrode morphology should satisfy certain criteria. This can be understood by considering the characteristic utilization length l_δ , defined as:

$$l_\delta = \sqrt{\frac{D_{ef} c_O x_\delta^0}{4a\Re_O}} \quad [5]$$

l_δ should be substantially smaller than the electrode thickness, in order to agree with the ALS model assumption of a semi-infinite electrode. On the other hand, if l_δ is comparable or lower than the size of some morphological features, e.g. the average particle diameter, then the ALS model assumption of a 1D macrohomogeneous electrode is invalid. Then, the microstructure plays a large role in determining the overall performance of the cathode. So, for example, if the electrode microstructural parameters (ε , a and τ) are known along with the material’s oxygen kinetic coefficients, then the ALS model can be used to predict the impedance response. Conversely, if the EIS response is measured and the microstructural parameters are known, then \Re_O and D_δ can be obtained from Eq. 2 and 3. This is the strategy employed by Lu, et al.⁹ and in the present paper. In either approach, the impedance response should be measured under conditions where the utilization length satisfies the above criteria relative to electrode morphology.

ALS model for O-interstitial conductors.— The ALS model was developed and has been applied to MIEC materials where oxygen vacancies are the responsible of the ionic conductivity.^{8–10,37} In particular, it has been applied successfully to determine the kinetic parameters (\Re and D) for the oxygen vacancy MIEC, $\text{La}_{1-x}\text{Sr}_x\text{CoO}_{3-\delta}$ (LSC).⁹ This section describes the modification to the ALS model for the case of MIEC materials in which ionic conductivity is dominated by interstitial oxygen, such as $\text{Nd}_2\text{NiO}_{4+\delta}$,²⁹ whereas the electronic conductivity is by electron-hole charge carriers.³³ The same model given above, i.e. Eq. 1–3 are used, but the parameters in these expression must be modified to properly describe the oxygen transport processes for interstitials. The oxygen defect structure and the thermodynamics behind the defect reaction are considered by analyzing the mechanism of oxygen hyper-stoichiometry formation:



where s_i is an empty interstitial site, O_i'' is an oxygen located on the interstitial site and h^\cdot is an electron hole. The crystal electro-neutrality imposes that $2c_{O_i''} = c_{h^\cdot}$.

One important term in the ALS model is the thermodynamic factor A_O describing the uptake/loss of oxygen by the MIEC upon changes in oxygen chemical potential. Considering the equation of defect formation Eq. 6, the oxygen chemical potential (μ_{O_2}) in equilibrium is given by

$$\mu_{O_2} = \mu_{\delta}^o + 2RT \ln \frac{c_{O_i''}}{c_{s_i}} + \frac{4c_{h^\cdot}}{g(E_F)} \quad [7]$$

where μ_{δ}^o is the standard chemical potential of defect formation, the second term of the equation is the contribution of configurational entropy of defects and the third term considers the change in energy due to the change of the electronic carrier concentration. $g(E_F)$ is the density of electronic states in the frame of the Rigid Band Formalism (RBF),³⁸ which should be calculated for $Nd_2NiO_{4+\delta}$ by using thermodynamic information such as that reported by Nakamura, et al.²⁰

The thermodynamic factor in the case of O-interstitials defects (see Eq. 4), can be determined by considering the variation of oxygen chemical potential with the mole fraction of oxygen defect (x_{δ}). To obtain the relationship between the mole fractions of oxygen interstitials (x_{δ}) and the empty interstitial sites (x_{s_i}) with the oxygen hyper-stoichiometry (δ), it is necessary to examine the crystal structure of the $Nd_2NiO_{4+\delta}$. Figure 1 shows the characteristic unit cell for orthorhombic $Nd_2NiO_{4+\delta}$ (space group $Fmmm$). The oxygen interstitial sites are indicated as tetrahedra coordinated by Nd atoms in the NdO layers. The NiO_6 octahedra are indicated in the $NdNiO_3$ layers. There are four formula units $Nd_2NiO_{4+\delta}$ in the unit cell and eight interstitial sites available for oxygen diffusion. Then, the molar concentrations (and the equilibrium mole fractions) for the empty oxygen interstitial lattice sites and the oxygen interstitials filled are given by $c_{s_i} = \frac{8-4\delta}{V_{u.c.}}$ ($x_{s_i}^0 = 1 - \delta/2 \approx 1$) and $c_{O_i''} = \frac{4\delta}{V_{u.c.}}$ ($x_{\delta}^0 = \delta/2$) respectively. Therefore, by combining Eq. 4 and 7 with the expression derived for each specie concentrations, the thermodynamic factor can be expressed as

$$A_O = 1 + \frac{4x_{\delta}}{RTg(E_F)} \quad [8]$$

Similar to the case of the 1D macrohomogeneous assumption for a MIEC electrode where the O diffusion is dominated by an oxygen vacancy mechanism,¹⁰ the electrode reaction in a porous electrode where the O-interstitials diffuse through the mixed conductor and the exchange of oxygen takes place at the gas/mixed-conductor interface is described by the equation

$$(1 - \epsilon) \frac{\partial c_{O_i''}(y, t)}{\partial t} = \frac{(1 - \epsilon)}{\tau_s} A_O D_{\delta} \frac{\partial^2 c_{O_i''}(y, t)}{\partial y^2} - ar \quad [9]$$

where $c_{O_i''}(y, t)$ is the displacement of the O-interstitial concentration from its value in the absence of a current when a current perturbation is applied (a.c. perturbation in the case of impedance measurements), y is the coordinate along the electrode thickness, and r is the oxygen surface exchange rate. Moreover, the oxygen surface exchange rate can be described as:³⁷

$$r = \Re_O (1 - e^{-\frac{\Lambda}{RT}}) \quad [10]$$

where Λ is the free-energy driving force for the step controlling the surface process, i.e. adsorption, incorporation. Then, a Gerischer-type impedance element is obtained, similar to that described by Eq. 1–3, using Eq. 9. Thus, EIS data fit to a Gerischer circuit element can be directly related to the kinetic parameters D_{δ} and \Re_O .

Experimental

Nickelate synthesis.— The NNO powder was synthesized by a sol-gel route. Nd_2O_3 and $Ni(CH_3COO)_3 \cdot H_2O$ were dissolved with acetic acid, hexamethylenetetramine (HMTA) and acetylacetone, using a ligand to metal molar ratio of 3:1. The solution was heated

until a gel was formed, which was then fired at 400°C. The powder was additionally calcined at 950°C for 12 h to eliminate any remaining impurity phases. No secondary phases were observed by powder X-ray diffraction (XRD). The compatibility between NNO and $La_{0.9}Sr_{0.1}Ga_{0.8}Mg_{0.2}O_{2.85}$ (LSGM) electrolytes was also checked by XRD similarly to a previous study of chemical reactivity between NNO and a $Ce_{0.9}Gd_{0.1}O_{1.95}$ (CGO) electrolyte.¹² No evidence of any chemical reaction was detected through XRD measurements of a NNO-LSGM powder mixture that had been heated at 1000°C for 72 h.

Symmetrical cell fabrication.— LSGM electrolyte pellets were formed by sintering LSGM powder (FuelCell Materials) at 1500°C for 4 h. NNO powders were suspended with polyvinyl butyral (2 wt%), polyethyleneglycol (1 wt%), ethanol (30 wt%) and α -terpineol (27 wt%), which were then deposited onto the LSGM pellets by spin coating. These electrodes were allowed to dry before being fired at 1000°C for 1 h in laboratory air. Gold metal grids were applied as current collectors for electrochemical testing.

Impedance testing and fitting.— EIS was measured for temperatures ranging from 500–700°C by using a frequency response analyzer (FRA) coupled to an AUTOLAB potentiostat. At 500, 600 and 700°C, the impedance response was evaluated as a function of oxygen partial pressure (pO_2) between $5.5 \cdot 10^{-4}$ and 1 atm. The pO_2 was controlled and sensed using an electrochemical gas blending system consisting of a zirconia pump and oxygen sensor³⁹ coupled to the impedance test system. The EIS spectra were fit using an electrical equivalent circuit with an inductor (L) in series with a resistor (R_{el}) and a Gerischer-type element (Z_G) applying a MatLab code.⁴⁰

FIB-SEM tomography.— In order to perform the microstructural evaluations, the symmetrical cells were broken into pieces after EIS measurement, followed by vacuum-infiltration with Buehler Epo-Thin epoxy at 50 mbar to fill open pores in the electrodes. The resultant epoxy pucks were then cut into small cubes and hand-polished to expose a cross-section of electrode material, down to a 1 μ m diamond suspension. The specimens were then affixed to a SEM stub sample holder with a cyanoacrylate glue.

Focused ion beam-scanning electron microscope (FIB-SEM) serial sectioned tomographic data sets were collected on a Zeiss 1540 XB. XY (image) resolution was 20 nm, based on an estimate of the average particle size of the sample. Z (slice thickness) resolution was 40 nm. The total reconstruction volume was 1075 μ m³. Segmentation of the two phases – NNO and epoxy filled pore – was completed on an image-by-image basis, performed with the Expectation Maximization/Maximization of Posterior Marginals (EM/MPM) technique, accomplished using the BlueQuartz Workbench open source GUI.⁴¹

Determination of phase volume percent and surface area were done using in-house developed codes, by voxel counting and a modified marching cubes algorithm, respectively.⁴² Tortuosity of the NNO phase was calculated by determination of the quasi-Euclidean distance of each NNO labeled voxel to a seed plane at each reconstruction voxel face, consisting only of segmented NNO voxels.⁴³ The pathway for each distance calculation was restricted to travel only through NNO voxels, and thus any isolated voxels are neglected. Tortuosity values, $T_s = \frac{L_{eff}}{L} = \sqrt{\tau_s}$, were determined by normalizing the calculated shortest distance by the seed plane normal distance for each NNO voxel in both directions along each principle axis of the reconstruction volume. The mean of the tortuosity values was then calculated for use in the ALS model. A cumulative particle size distribution of the NNO phase was also calculated using Holzer's method in three dimensions.⁴⁴ This method is a virtual analog of mercury porosimetry, where a Euclidean distance map is constructed such that each NNO labeled voxel is assigned the distance to the nearest non-NNO labeled voxel. This structure is then queried to determine the total volume which can be accessed by spheres of successively larger radius. The

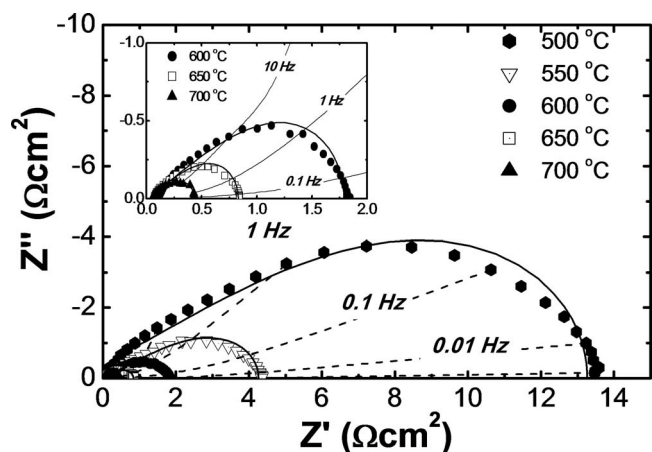


Figure 2. Electrochemical impedance spectra at different T in air for $\text{Nd}_2\text{NiO}_{4+\delta}$ electrode deposited on LSGM electrolyte. Solid lines represent the arcs resulting of fitting data with a Gerischer-type element. Dashed lines indicating the same frequency are included as a guide to the eyes.

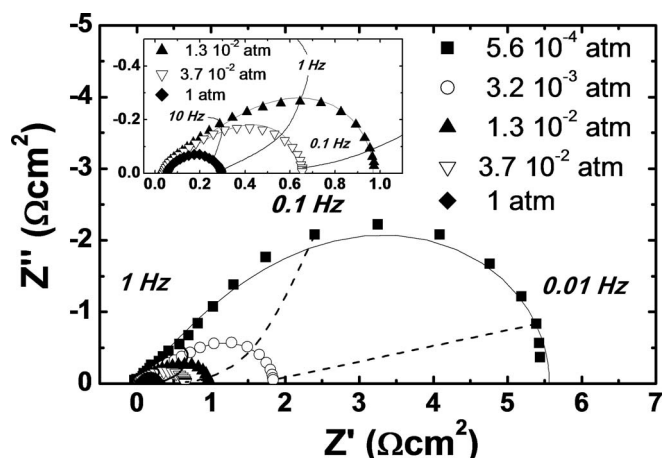


Figure 3. Impedance spectra obtained at 700 °C at different $p\text{O}_2$. Solid lines represent the arcs resulting of fitting data with a Gerischer-type element. Dashed lines indicating the same frequency are included as a guide to the eye.

sphere radii can be increased with sub-pixel resolution precision to produce as accurate a distribution as possible.

Results and Discussion

Electrochemical response.— Figure 2 shows typical examples of impedance spectra (data points) measured as a function of temperature for the symmetrical cell $\text{Au}/\text{NNO}/\text{LSGM}/\text{NNO}/\text{Au}$. The data, collected at temperatures ranging between 500 and 700 °C in 0.2 atm O_2 , are normalized to the geometric area of the electrodes in the symmetrical cell. Figure 3 shows representative impedance spectra recorded at 700 °C and $p\text{O}_2$ ranging between $5.6 \cdot 10^{-4}$ to 1 atm. Both figures also show the fits obtained using Gerischer-type elements (solid lines). Reasonably good fits are obtained with this single element over a wide range of temperatures and $p\text{O}_2$ values. One exception is the highest temperature and lowest $p\text{O}_2$, where the arc does not have the Gerischer shape predicted by the ALS model, for reasons that will be explained in terms of utilization length below. Figure 4a and 4b show the Gerischer resistance (R_G) and time constant (τ_G) values obtained from the fitted Gerischer responses, plotted versus T^{-1} . The data points fit well to an Arrhenius-type dependency (solid line) giving overall activation energies $E_a = 1.09 \pm 0.02$ eV for R_G and $E_a = 1.1 \pm 0.1$ eV for τ_G .

Figures 5a and 5b show log-log plots of R_G and τ_G versus $p\text{O}_2$, respectively. The power laws $R_G \propto (p\text{O}_2)^{-0.25}$ and $\tau_G \propto (p\text{O}_2)^{-0.5}$, are also shown, and are in fairly good agreement with the data over part of the pressure range. These are the expected dependences based on

the ALS model, and are discussed in a following section. The slope changes at high temperature and low $p\text{O}_2$, which may be related to the utilization length becoming comparable to the electrode thickness, as will be discussed below.

Microstructural analysis.— Figure 6 illustrates a 3D image representation of the entire structure (a), a magnified 3D view of a portion of the structure (b), and a typical 2D section of the measured electrode microstructure (c). The structure is typical of SOFC cathode electrodes produced by firing of particle compacts, showing reasonably uniform particle sizes and good necking between particles.⁸ Analysis of the 3D data yields the parameters needed for ALS model analysis: solid phase fraction $\varepsilon = 0.46$, a specific surface area $a = 4.96 \mu\text{m}^{-1}$, and a solid phase tortuosity factor of 1.181. Also, no closed porosity was observed, not surprising given the high pore volume fraction. Figure 6d shows the cumulative particle size distribution of the NNO phase, showing a mean particle size of 320 nm.

Kinetic parameters and validation of method.— The impedance results and morphological features presented above can be combined using Eq. 2, 3, and 8 to obtain the diffusion coefficient and the molar surface rate for O-interstitial defects. The thermodynamic factor was calculated from Eq. 8 by using the density of states estimated from Nakamura, et al.²⁰ data and the oxygen content measured in this work. Then, the density of states ($g(E_F) = 0.007(\text{kJmol}^{-1})^{-1}$) was estimated from the thermodynamic data of oxygen content for $\text{Nd}_2\text{NiO}_{4+\delta}$ obtained by thermo-gravimetry

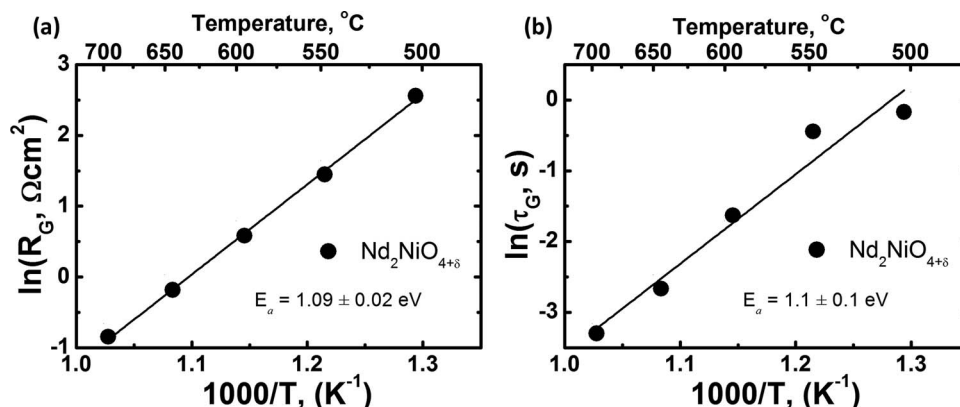


Figure 4. Arrhenius plot for (a) the Gerischer resistance (R_G) and (b) the time constant (τ_G). The activation energies are indicated on the graphs.

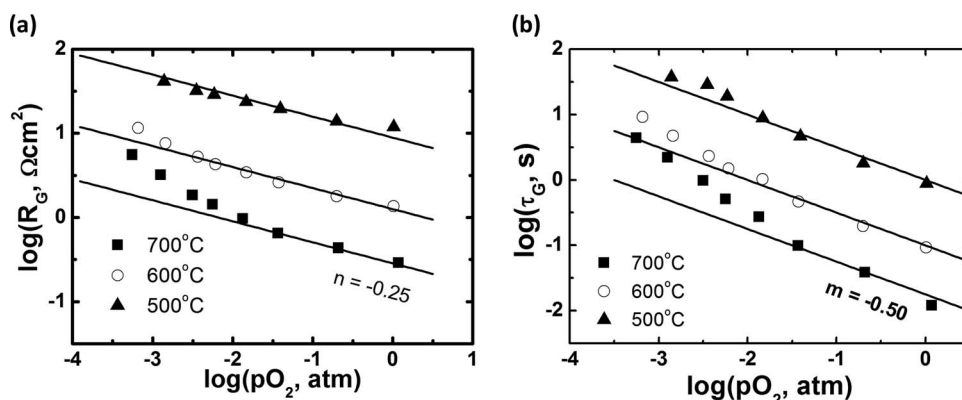


Figure 5. log-log graphic for (a) Gerischer resistance (R_G) and (b) Gerischer time constant (τ_G) with $p\text{O}_2$ at 500, 600 and 700°C. Solid lines indicate the expected $p\text{O}_2$ dependency, $R_G \propto (p\text{O}_2)^{-0.25}$ and $\tau_G \propto (p\text{O}_2)^{-0.5}$ from the proposed model.

and coulometric titration between 600–900°C and $p\text{O}_2$ between 10^{-10} – 10^0 atm²⁰ using the same procedure as in others perovskite-type materials.^{38,45,46} The equilibrium oxygen hyper-stoichiometry (δ) for the present $\text{Nd}_2\text{NiO}_{4+\delta}$ powder was measured in this work as a function of temperature, in air, by thermogravimetry (TG) using a symmetrical thermobalance based on a Cahn 1000 electrobalance. Table I presents these values, which were used to adjust and extend the Nakamura data to different temperature and $p\text{O}_2$ values, the Nakamura data in air at 600 and 700°C and A_O calculated from Eq. 8. NNO lattice parameters were obtained from XRD and give a unit cell volume $V_{\text{u.c.}} = 218.3 \text{ cm}^3 \text{ mol}^{-1}$. Figure 7 shows the resulting plots of D_δ and \mathfrak{R}_O versus inverse temperature in air. Both quantities fit well with an Arrhenius dependency yielding the activation energies shown. Figure 8 shows the dependency of these coefficients on $p\text{O}_2$ and Table II describes the main characteristic of D_δ and \mathfrak{R}_O for the NNO porous electrode.

At this point, it is possible to examine the ALS model assumptions of a 1D macrohomogenous and semi-infinite porous electrode. To validate this assumption, the characteristic utilization length l_δ given should be higher than the characteristic electrode length scale, i.e.

Table I. Oxygen hyper-stoichiometry for $\text{Nd}_2\text{NiO}_{4+\delta}$ determined by TG analysis and thermodynamic factor A_O calculated from Nakamura data.²⁰

T (°C)	500	550	600	650	700
δ^\dagger	0.203	0.195	0.179	0.173	0.167
δ^\ddagger			0.138		0.124
A_O	6.9	9.1	8.0	7.4	6.9

[†]from TG data of this work,

[‡]from TG data of Nakamura et al.²⁰

the average particle diameter of 320 nm, and lower than the electrode thickness of $\sim 10 \mu\text{m}$ (see Figure 6). Figure 9 shows l_δ versus temperature and $p\text{O}_2$ derived from the present data using Eq. 5. In these figures a straight line indicating the average particle size is also included. l_δ increases as $p\text{O}_2$ decreases, similarly to that reported in the case of LSC, an O-vacancy bulk diffusion material.⁹ As the average particle size is lower than l_δ , application of the ALS model is suitable over

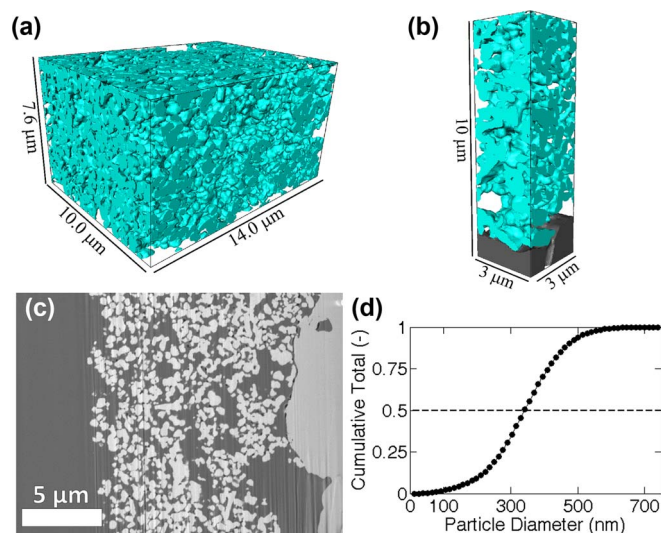


Figure 6. (a) 3D reconstruction obtained from FIB-SEM tomography. (b) Selected region with portion of electrolyte, to give a sense of similarity to the model geometry of the ALS model. (c) Representative 2D section from the 3D data set. (d) Cumulative particle size distribution of the solid NNO phase as calculated by Holzer's method. The distribution is monodisperse, as there are no secondary plateaus present. The midpoint, at ~ 320 nm, is the average particle size, with most particles falling within ± 100 nm of this size.

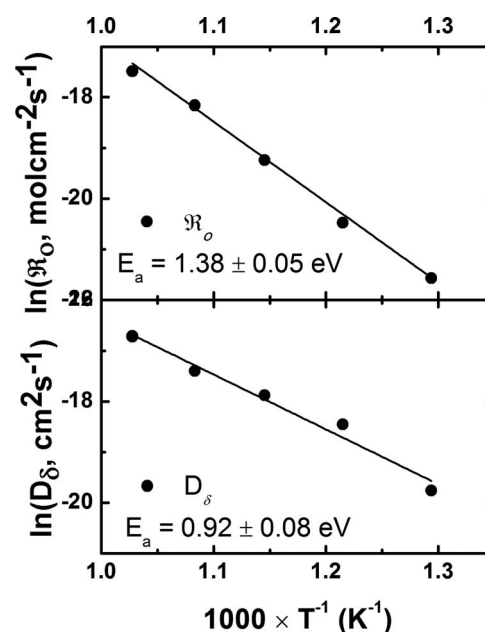


Figure 7. Arrhenius plot for the O-interstitials \mathfrak{R}_O and D_δ coefficients, in air, obtained by combining Gerischer resistance and time constant with microstructural features and thermodynamics data.

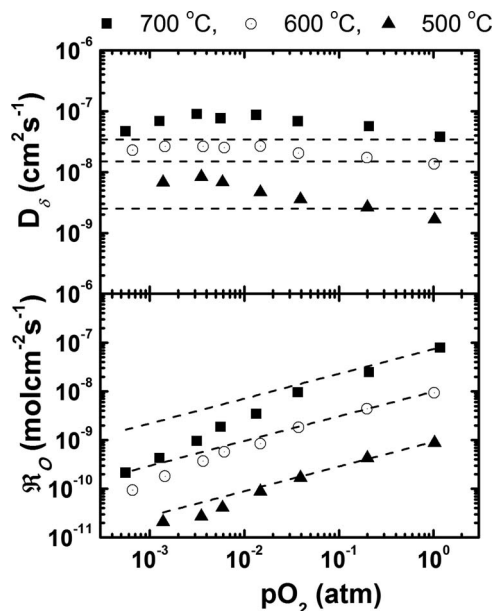


Figure 8. O-interstitial diffusion coefficient D_δ and molar surface exchange rate \mathfrak{M}_O vs pO_2 , log-log plot at 500, 600 and 700°C. Dashed lines indicate the expected pO_2 dependency, $D_\delta \propto (pO_2)^0$ and $\mathfrak{M}_O \propto (pO_2)^{-0.5}$ from the proposed model.

most of the measured parameters; the exception is for low pO_2 values, where l_δ reaches $\sim 10 \mu m$, comparable with the electrode thickness, invalidating the semi-infinite electrode assumption. This may explain the non-Gerischer shape of the arc at 700°C and low pO_2 in Figure 3.

Within the above-described range of validity of the model, the pO_2 dependency of both kinetics parameters can be extracted. It may be possible to obtain insights into the surface exchange process mechanism by analyzing the pO_2 dependency of \mathfrak{M}_O in Figure 8, and to obtain the corresponding kinetic coefficient k_{chem} . For the analysis, a bulk transport path for oxygen diffusion is assumed, supported by the weak pO_2 dependency of NNO diffusion coefficient with pO_2 .⁹

The oxygen surface exchange involves a series of steps such as adsorption of O_2 molecules from gas phase, dissociation of these molecules and incorporation of the O-atoms into the MIEC bulk. The above processes alter the configurational molar entropy (s_{conf}) of the system and, because they should include a charge transfer process, they also affect the non-ideal molar enthalpy (h_n) because the electron density of the oxide is changing. Then the driving force for each individual step (Δ_j) can be described based on non-equilibrium thermodynamics as the difference of chemical potential of the reaction step:³⁷

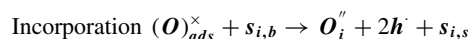
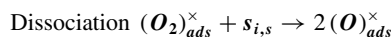
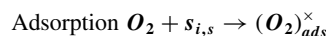
$$\Delta_j = \Delta\mu_j = \Delta\mu_j^0 + (T\Delta s_{conf} + \Delta h_n)_j^* \quad [11]$$

The linearization of Eq. 10 allows calculation of the molar exchange rate as

$$\begin{aligned} \mathfrak{M}_O &= \lambda RT \left(\frac{\partial r}{\partial \Lambda} \right)_T = \lambda RT \left(\frac{\partial r}{\partial \ln x_\delta} \right)_T \left(\frac{1}{\left(\frac{\partial \mu}{\partial \ln x_\delta} \right)_T} \right) \\ &= -\lambda \frac{x_\delta}{A_O} \left(\frac{\partial r}{\partial x_\delta} \right)_T \end{aligned} \quad [12]$$

Where λ is a stoichiometric factor, A_O is the thermodynamic factor, and x_δ is the mole fraction of the active species (O-interstitial) which changes with pO_2 .

A mechanism similar to that proposed by Adler, et al.³⁷ for $La_{1-x}Sr_xCoO_{3-\delta}$ (LSC) oxygen surface exchange mechanism can be here applied. However, whereas LSC surface exchange involves the O_2 surface adsorption and dissociation in O vacancy surface sites followed by O-incorporation in a bulk O-vacancy, an oxygen surface vacancy should not necessarily be required for NNO, as the O-incorporation could involve either an empty O-interstitial site on the NdO layer or an O-vacancy site on the perovskite layer. One possible mechanism for the overall reaction Eq. 6 consists of the following individuals steps:



where $(O)_{ads}^\times$ refers to molecular or atomic O-adsorbed species. $s_{i,s}$ and $s_{i,b}$ are empty sites to O-interstitial incorporation at surface and interior of solid, respectively. The O-interstitial defects are denoted as O_i'' and, as the NNO is a p-type conductor, the charge transfer process involves electron-hole charge carriers h^\cdot . The \mathfrak{M}_O variation with pO_2 can be derived from Eq. 12. Assuming, for example, adsorption and dissociation under steady-state, that means the driving force $\Lambda_1 = \Lambda_2 = 0$, and therefore the oxygen surface exchange is controlled by O-incorporation with a rate given by

$$\begin{aligned} r &= k(T) \Gamma_{(O)_{ads}^\times} c_{s_i} = k'(T) (pO_2)^{1/2} \Gamma_{s_{i,s}} c_{s_i} \\ &\approx k'(T) (pO_2)^{1/2} \frac{8(1-x_\delta)}{V_{u.c.}} \end{aligned} \quad [13]$$

Using Eq. 13 in Eq. 12, the molar exchange rate can be expressed as

$$\mathfrak{M}_O = \frac{k_{chem}}{A_O} (pO_2)^{1/2} x_\delta \frac{8}{V_{u.c.}} \quad [14]$$

where k_{chem} is the chemical surface exchange coefficient. Figure 8 shows the fit of \mathfrak{M}_O with Eq. 14. Although the pO_2 dependency of x_δ and A_O has been included in these lines, note that these are relatively weak so they follow quite close to $(pO_2)^{1/2}$. This dependency fits well

Table II. Brief description and comparison between oxygen diffusion coefficient (D_δ) and molar surface exchange rate (\mathfrak{M}_O) obtained by applying ALS model to $La_{0.8}Sr_{0.2}CoO_{3-\delta}$ (LSC-82), $La_{0.6}Sr_{0.4}CoO_{3-\delta}$ (LSC-64) and $Nd_2NiO_{4+\delta}$ (NNO).

		Kinetics parameters at 700°C - 1 atm		
	O conducting specie	D_δ (cm ² s ⁻¹)	\mathfrak{M}_O (molcm ⁻² s ⁻¹)	Ref.
NNO	O-interstitials O_i''	$D_\delta = 3.7 \cdot 10^{-8}$ $E_a = 0.92$ eV Weakly pO_2 dependent	$\mathfrak{M}_O = 7.9 \cdot 10^{-8}$ $E_a = 1.38$ eV Power-law dependency on pO_2	This work
LSC-82	Surface O-vacancies V_O^\bullet	$D_\delta = 10^{-6}$ pO_2 dependent	$\mathfrak{M}_O = 10^{-8}$ Almost pO_2 independent	9
LSC-64	Bulk O-vacancies V_O^\bullet	$D_\delta = 10^{-7}$ $E_a = 1.5$ eV Weakly pO_2 dependent	$\mathfrak{M}_O = 1.5 \cdot 10^{-7}$ $E_a = 0.46$ eV Power-law dependency on pO_2	9

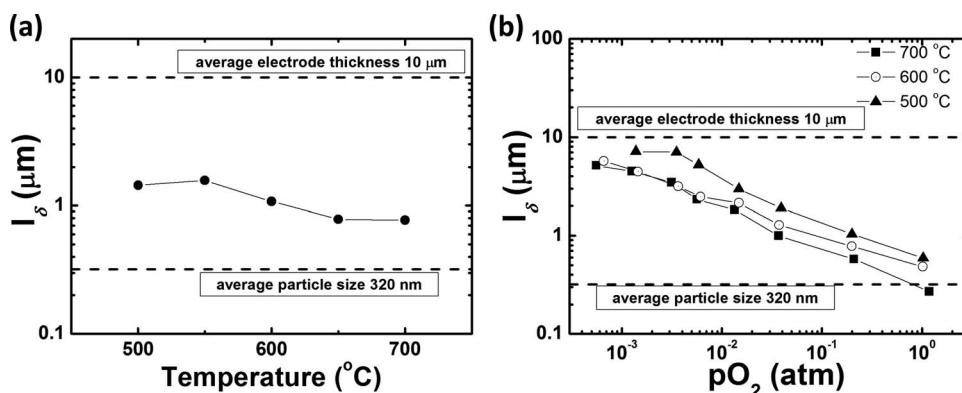


Figure 9. Characteristic utilization length l_δ obtained from ALS model as a function of (a) T in air and (b) $p\text{O}_2$ at 500, 600 and 700 $^\circ\text{C}$. Dashed lines indicate the average particle size and electrode thickness obtained from FIB-SEM analysis.

to the data, except at low $p\text{O}_2$ and high T. From this fitting, average k_{chem} values of $7.0 \cdot 10^{-4}$, $1.8 \cdot 10^{-5}$ and $1.9 \cdot 10^{-6} \text{ cm} \cdot \text{s}^{-1}$ have been found at 700, 600 and 500 $^\circ\text{C}$, respectively. Figure 10 shows the individual k_{chem} values as a function of $p\text{O}_2$ at 500, 600 and 700 $^\circ\text{C}$, obtained using Eq. 14 and the data in Figure 8, and the comparison with the average values. From this comparison, it can be observed that k_{chem} is almost independent with $p\text{O}_2$ over part of the measured parameter range, in agreement with our surface exchange model. It should be noted, however, that a similar $p\text{O}_2$ dependency may arise from other mechanisms, so the agreement does not necessarily imply that incorporation is the rate limiting step. To make a complete assignment of the true surface reaction mechanism, additional information, such as nonlinear kinetics and detailed surface structure, will be needed. On the other hand, Figure 10 shows a deviation of the expected behavior at high T and low $p\text{O}_2$, similar to that observed for the Gerischer resistance and time constant in Figure 5 and \mathfrak{R}_O in Figure 8. As suggested above, these deviations from the model might be explained by a deviation from the electrode semi-infinite assumption. Alternatively, the deviations may arise in part from the assumption that incorporation is rate limiting, with adsorption and dissociation processes being fast, which may become invalid at low enough $p\text{O}_2$.

At high temperature, the O-interstitial diffusion coefficient is nearly independent of $p\text{O}_2$ in Figure 8 as expected for bulk diffusion mechanism in an interstitial conductor, since the interstitial concentration varies relatively little over this range of $p\text{O}_2$ values. The increase in the diffusion coefficient with decreasing $p\text{O}_2$ at 500 $^\circ\text{C}$ may suggest a contribution of surface diffusion. Observing the correct dependency over a wide range of measurements helps to validate the present results and analysis. Substituting Eq. 14 in Eq. 2 and 3, and assuming weak variations of x_δ , D, and A_O with $p\text{O}_2$, the $p\text{O}_2$ dependences R_G

$\propto (p\text{O}_2)^{-0.25}$ and $\tau_G \propto (p\text{O}_2)^{-0.5}$ are obtained. These values are in approximate agreement with the slopes fitted to the measured $p\text{O}_2$ dependences in Figures 5a and 5b. The deviations from these predicted slopes at low $p\text{O}_2$ are probably related to the deviation from the semi-infinite electrode assumed in the ALS model, because of the utilization lengths becoming comparable to the electrode thickness, as discussed above (see Figure 9b).

The present surface exchange and the diffusion coefficient results can be compared with prior measurements utilizing relaxation techniques 4 and isotope exchange depth profiling (IEDP) coupled to SIMS 1. Each technique gives a different kind of coefficient, chemical coefficients (D_{chem} and k_{chem}) or tracer coefficients (D^* and k^*) which are related by the following expressions:

$$D_\delta = \frac{D^*}{x_\delta^0} = \frac{D_{\text{chem}}}{A_O} \quad [15]$$

$$k_\delta = \frac{k^*}{x_\delta^0} = \frac{k_{\text{chem}}}{A_O} \quad [16]$$

Figure 11 shows the comparison between D_δ and k_δ obtained in this work for $\text{Nd}_2\text{NiO}_{4+\delta}$ and those previously reported from conductivity relaxation, $D_{\text{chem}} = D_\delta A_O$ ^{24,26} and from IEDP by SIMS $D^* = D_\delta x_\delta^{0.23}$ using the x_δ^0 and A_O reported in this work in combination with the D^* , k^* , D_{chem} and k_{chem} values reported in those works. There are a clear difference among the D_δ and k_δ values obtained using the present method and the previously reported methods.

The present method has some potential advantages regarding accuracy and convenience of measurement. First, the preparation of materials is similar to that used in full fuel cell fabrication, ensuring that the material's surface and microstructure is similar to that of typical electrodes. New fabrication methods, such as that for dense pellets, are not required, and effects introduced at high densification temperatures such as changes in surface composition, are not present. These effects can modify the exchange rate coefficients by an order of magnitude.⁴⁷ Second, as long as the utilization length falls between the electrode thickness and the particle size, the co-limited nature of the electrode process ensures that both D_δ and k_δ contribute substantially. Thus, both coefficients can be measured with good accuracy from a single sample. In IEDP and conductivity relaxation measurements, the sample dimensions might not match well with the characteristic length scale. Dense bulk samples must be large enough to prevent the crossing of the concentration profiles in the center of it during the tracer annealing time.¹ Further, the smallest dimension of IEDP or conductivity relaxation samples should be close to the characteristic distance D/k . If the ratio D/k is much lower than the dimensions of the dense sample, then the results for D are accurate but k will have considerable error. This is the case, for example, for the NNO data reported by Egger, et al.,^{24,26} where the D/k values ranging from 0.04 and 0.1 mm are lower than the shortest sample dimension

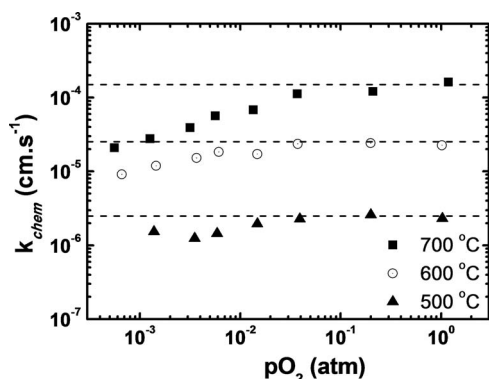


Figure 10. Chemical surface exchange coefficient for O-interstitial incorporation as a function of $p\text{O}_2$ at 500, 600 and 700 $^\circ\text{C}$. Dashed lines indicate the average k_{chem} values obtained from fitting \mathfrak{R}_O with the proposed model.

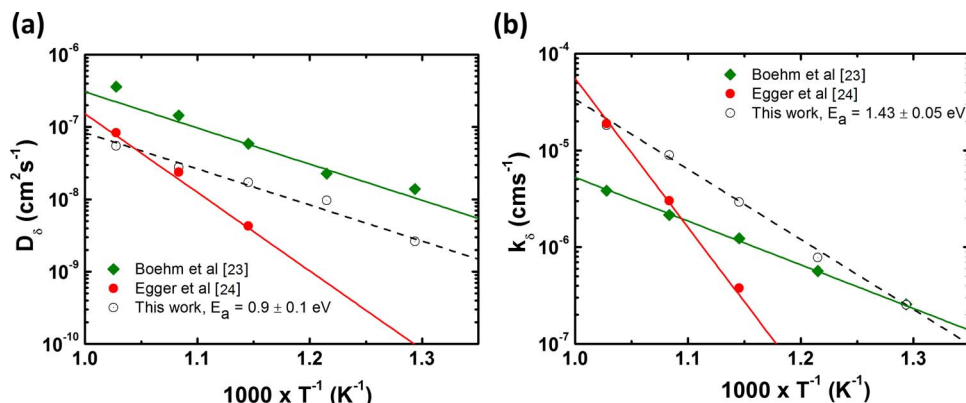


Figure 11. Comparison between D_δ (a) and k_δ (b) obtained in this work and those reported from isotope exchange depth profile by SIMS²³ and conductivity relaxation.²⁴

(1 mm). Conversely, if D/k is larger than sample dimension, then k can be obtained accurately but D will have considerable inaccuracy.⁴ For conductivity relaxation measurements of porous samples, accuracy in determination of D and k depends heavily on the sample thickness.⁷ Furthermore, the particle size for this method is typically much larger than D/k , such that it can be difficult for k to be measured accurately. Thus, it may be necessary in IEDP and conductivity relaxation to employ multiple samples with different dimensions to obtain kinetic parameters over the range of temperatures and $p\text{O}_2$ values of interest.

The results obtained in this work can be compared with those obtained for $\text{La}_{0.8}\text{Sr}_{0.2}\text{CoO}_{3-\delta}$ (LSC-82) and $\text{La}_{0.6}\text{Sr}_{0.4}\text{CoO}_{3-\delta}$ (LSC-64) porous electrodes where a similar approach combining EIS and microstructural data was applied.⁹ Lu, et al.⁹ concluded that, whereas the O-vacancy diffusion in LSC-64 is consistent with a bulk transport path, LSC-82 could be understood assuming a parallel surface transport path, where surface mobility is governed by some kind of interstitial or adatom diffusion mechanism. These LSC electrodes exhibit porosity values of 0.55, tortuosity assumed equal to 1 and specific surface area of $2.8 \mu\text{m}^{-1}$ and $6.2 \mu\text{m}^{-1}$ for LSC-82 and LSC-64, respectively. Besides compiling D_δ and \mathfrak{H}_O results for NNO, Table II also gives a comparison to LSC-82, and LSC-64 results obtained by applying the ALS model. As mentioned before, the weak $p\text{O}_2$ dependency of NNO diffusion coefficient suggests a bulk transport path as in the case of LSC-64 electrode. A noticeable difference between NNO and LSC-64 electrode kinetics is the higher activation energy for the O-surface exchange rate \mathfrak{H}_O in the NNO. In addition, the diffusion coefficient and the molar exchange rate for NNO are lower than those for LSC perovskites at 700°C . In spite of this, and due to the lower volumetric defect concentration, the exchange rate coefficients k_δ obtained for NNO ($\sim 10^{-5} \text{ cm} \cdot \text{s}^{-1}$ at 700°C) electrodes are effectively higher than those of lanthanum-strontium cobaltites ($\sim 10^{-6} \text{ cm} \cdot \text{s}^{-1}$ at 750°C), ferrites ($\sim 10^{-6} \text{ cm} \cdot \text{s}^{-1}$ at 750°C) or manganites ($\sim 10^{-8} \text{ cm} \cdot \text{s}^{-1}$ at 750°C) and comparable to those of faster surface exchange materials, such as $\text{Ba}_{1-x}\text{Sr}_x\text{Co}_y\text{Fe}_{1-y}\text{O}_{3-\delta}$ ($\sim 10^{-4}$ – $10^{-5} \text{ cm} \cdot \text{s}^{-1}$ at 750°C).⁴⁸

Conclusions

The ALS model, describing the impedance response for a macro-homogenous semi-infinite porous electrode, can be successfully applied to an O-interstitial defective oxide such as the $\text{Nd}_2\text{NiO}_{4+\delta}$ nickelate. The O-kinetic parameters such as O-bulk diffusion coefficient and surface exchange rate can be obtained as a function of temperature and $p\text{O}_2$ by combining the electrochemical impedance response with the microstructural parameters and taking care of the proper use of thermodynamic factors for this kind of defects. Then, from EIS data recorded as a function of temperature and $p\text{O}_2$ and 3D FIB-SEM microstructural reconstruction of the porous electrode, the electrochemical response can be modeled in a wide range of temperature and $p\text{O}_2$ by considering a co-limiting process governed by O-incorporation

and O-interstitial bulk diffusion. However, some limitations of this method should be considered such as in the range of validity of the ALS model. The utilization length must be larger than the average particle size but smaller than the electrode thickness for assumptions of the model to hold.

At 700°C , the D_δ and \mathfrak{H}_O obtained for $\text{Nd}_2\text{NiO}_{4+\delta}$ are lower than those of Co-rich perovskites such as $\text{La}_{0.8}\text{Sr}_{0.2}\text{CoO}_{3-\delta}$ and $\text{La}_{0.6}\text{Sr}_{0.4}\text{CoO}_{3-\delta}$. However, the low activation energy for O-diffusion, along with the nature of interstitial defects which increase their concentration as temperature decreases, guarantees a lower contribution of diffusion to polarization resistance at low temperatures, as compared with LSC electrodes. The high molar surface exchange rate activation energy can be mitigated by improving the microstructural design by increasing the specific surface area. Despite low molar exchange rates for NNO Ruddlesden-Popper phases as an effect of low volumetric defect concentration, the exchange rate coefficients k_δ are similar to those of faster exchange rate for state of art perovskites. Thus, nickelates can be suitable electrode materials for IT-SOFC by properly tuning their microstructure.

Finally, the comparison between the D_δ and k_δ coefficients here obtained and those previously reported from conductivity relaxation and isotope exchange depth profile (IEDP) by SIMS methods, allowed a critical analysis on the applicability and confidence of the different methodologies including the present work. Under properly selected experimental conditions, the method presented in this paper has the advantage of determination of kinetic coefficients of materials with the same microstructure as real electrodes.

Acknowledgments

The authors at Northwestern University gratefully acknowledge support by the US Department of Energy Basic Energy Science program (Grant # DE-FG02-05ER46255). FIB-SEM tomography data was collected at the Electron Microscopy Center at Argonne National Laboratory. The authors at Centro Atomico Bariloche appreciate the financial support of Comisión Nacional de Energía Atómica (CNEA), Consejo Nacional de Investigaciones Científicas y Técnicas (CONICET), Agencia Nacional de Promoción de Ciencia y Tecnología (AGNPCyT) y Universidad Nacional de Cuyo. L. Moggi is especially grateful to the Fulbright – CONICET Postdoc Grant Program.

List of Symbols

D	diffusion coefficient (in $\text{cm}^2 \text{s}^{-1}$)
D^*	O-isotope labeled or tracer diffusion coefficient
D_{chem}	chemical diffusion coefficient
D_δ	defect diffusion coefficients for O-vacancies or interstitials
D_{ef}	effective diffusion coefficients in porous material

k	surface exchange coefficient (in cm.s^{-1})
k^*	O-isotope labeled or tracer surface exchange coefficient
k_{chem}	chemical surface exchange coefficient
k_{δ}	O-defect surface exchange coefficient
\mathfrak{R}_{O}	O-defect (O-vacancies or O-interstitials) equilibrium molar surface exchange rate
r	oxygen surface exchange rate
δ	oxygen defects, vacancies or hyperstoichiometry.
p_{O_2}	oxygen partial pressure
Z_G	Grischer impedance
R_G	Gerischer resistance
τ_G	Grischer time constant
$V_{\text{u.c.}}$	unit cell volume
E_a	activation energy
c_{O}	Concentration of oxygen lattice sites involved in diffusion mechanism
x_{δ}^0	equilibrium fraction molar concentration of defects
A_{O}	$= \pm \frac{1}{2RT} \frac{\partial \mu_{\text{O}_2}}{\partial \ln x_{\delta}}$ thermodynamic factors for oxygen vacancies (−) or interstitials (+)
s_i	empty interstitial site
O_i''	interstitial oxygen
h^{\cdot}	electron hole
$c_{s_i}, c_{\text{O}_i''}$	molar concentrations of empty oxygen interstitial sites and oxygen interstitials
$\mu_{\text{O}_2}, \mu_{\delta}^0$	oxygen gas and reference defect chemical potentials
x_{δ}, x_{s_i}	mole fraction of oxygen interstitials and empty interstitial sites
ε	porosity
T_s	tortuosity
τ_s	tortuosity factor
a	specific surface area
Δ	free-energy driving force
$g(E_F)$	density of electronic states
l_{δ}	characteristic utilization length
h_n	molar enthalpy
λ	stoichiometric factor

References

- J. A. Kilner, S. J. Skinner, and H. H. Brongersma, *J. Solid State Electrochem.*, **14**, 861 (2011).
- E. N. Armstrong, K. L. Duncan, D. J. Oh, J. F. Weaver, and E. D. Wachsman, *Journal of The Electrochemical Society*, **158**, B492 (2011).
- L. Wang, R. Merkle, and J. Maier, *Journal of The Electrochemical Society*, **157**, B1802 (2010).
- J. A. Lane and J. A. Kilner, *Solid State Ionics*, **136**, 997 (2000).
- Y. Li, K. Gerdes, T. Horita, and X. Liu, *Journal of The Electrochemical Society*, **160**, F343 (2013).
- W. Preis, E. Bucher, and W. Sitte, *Journal of Power Sources*, **106**, 116 (2002).
- R. A. Cox-Galhotra and S. McIntosh, *Solid State Ionics*, **181**, 1429 (2010).
- C. R. Kreller, M. E. Drake, S. B. Adler, H.-Y. Chen, H.-C. Yu, K. Thornton, J. R. Wilson, and S. A. Barnett, in *SOFC-XII*, S. C. Singhal and K. Eguchi Editors, p. 815, ECS Conference Proceedings, Montreal (2011).
- Y. Lu, C. R. Kreller, and S. B. Adler, *Journal of The Electrochemical Society*, **156**, B513 (2009).
- S. B. Adler, J. A. Lane, and B. C. H. Steele, *Journal of the Electrochemical Society*, **143**, 3554 (1996).
- J. Wan, J. B. Goodenough, and J. H. Zhu, *Solid State Ionics*, **178**, 281 (2007).
- A. Montenegro-Hernández, L. Moggi, and A. Caneiro, *International Journal of Hydrogen Energy*, **37**, 18290 (2012).
- M. J. Escudero, A. Aguadero, J. A. Alonso, and L. Daza, *Journal of Electroanalytical Chemistry*, **611**, 107 (2007).
- F. Chauveau, J. Mougou, J. M. Bassat, F. Mauvy, and J. C. Grenier, *Journal of Power Sources*, **195**, 744 (2010).
- D. J. Chen, F. C. Wang, H. G. Shi, R. Ran, and Z. P. Shao, *Electrochim Acta*, **78**, 466 (2012).
- S. E. Hou, J. A. Alonso, and J. B. Goodenough, *Journal of Power Sources*, **195**, 280 (2010).
- S. P. Jiang, S. Zhang, and Y. D. Zhen, *Journal of The Electrochemical Society*, **153**, A127 (2006).
- D. Oh, E. Armstrong, D. Jung, C. Kan, and E. Wachsman, *ECS Transactions*, **25**, 2871 (2009).
- S. P. Simmer, M. D. Anderson, M. H. Englehard, and J. W. Stevenson, *Electrochemical and Solid-State Letters*, **9**, A478 (2006).
- T. Nakamura, K. Yashiro, K. Sato, and J. Mizusaki, *Journal of Solid State Chemistry*, **182**, 1533 (2009).
- N. Grunbaum, L. Moggi, F. Prado, and A. Caneiro, *Journal of Solid State Chemistry*, **177**, 2350 (2004).
- C. Munnings, S. Skinner, G. Amow, P. Whitfield, and I. Davidson, *Solid State Ionics*, **176**, 1895 (2005).
- E. Boehm, J. M. Bassat, P. Dordor, F. Mauvy, J. C. Grenier, and P. Stevens, *Solid State Ionics*, **176**, 2717 (2005).
- A. Egger, E. Bucher, W. Sitte, C. Lalanne, and J. M. Bassat, *ECS Transactions*, **25**, 2547 (2009).
- G. Garcia, M. Burriel, N. Bonanos, and J. Santiso, *Journal of The Electrochemical Society*, **155**, P28 (2008).
- A. Egger, E. Bucher, and W. Sitte, *Journal of the Electrochemical Society*, **158**, B573 (2011).
- Y. Toyosumi, H. Ishikawa, and K. Ishikawa, *Journal of Alloys and Compounds*, **408**, 1200 (2006).
- V. V. Vashook, I. I. Yushkevich, L. V. Kokhanovsky, L. V. Makhnach, S. P. Tolochko, I. F. Kononyuk, H. Ullmann, and H. Altenburg, *Solid State Ionics*, **119**, 23 (1999).
- M. Al Daroukh, V. V. Vashook, H. Ullmann, F. Tietz, and I. A. Raj, *Solid State Ionics*, **158**, 141 (2003).
- V. V. Kharton, A. P. Viskup, E. N. Naumovich, and F. M. B. Marques, *J Mater Chem*, **9**, 2623 (1999).
- H. Zhao, F. Mauvy, C. Lalanne, J. Bassat, S. Fourcade, and J. Grenier, *Solid State Ionics*, **179**, 2000 (2008).
- J. M. Bassat, P. Odier, A. Villesuzanne, C. Marin, and M. Pouchard, *Solid State Ionics*, **167**, 341 (2004).
- M. Zaghrifou, F. Giovannelli, N. Piro, D. Brouri, and I. Laffez, *Journal of Solid State Chemistry*, **177**, 3351 (2004).
- J. M. F. Chauveau, F. Mauvy, J. M. Bassat, and J. C. Grenier, *ECS Transactions*, **25**, 2557 (2009).
- S. B. Adler, *Chemical Reviews*, **104**, 4791 (2004).
- J. Fleig and J. Maier, *Journal of the European Ceramic Society*, **24**, 1343 (2004).
- S. B. Adler, X. Y. Chen, and J. R. Wilson, *J Catal*, **245**, 91 (2007).
- J. E. tenElshof, M. H. R. Lankhorst, and H. J. M. Bouwmeester, *Journal of The Electrochemical Society*, **144**, 1060 (1997).
- A. Caneiro, P. Bavadaz, J. Fouletier, and J. P. Abriata, *Review of Scientific Instruments*, **53**, 1072 (1982).
- J.-L. Dellis, Zfit, in, <http://www.mathworks.com/matlabcentral/fileexchange/19460-zfit> (2014).
- M. A. Groeber and M. A. Jackson, *Integrating Materials and Manufacturing Innovation*, **3** (2014).
- J. R. Wilson, M. Gameiro, K. Mischaikow, W. Kalies, P. W. Voorhees, and S. A. Barnett, *Microsc Microanal*, **15**, 71 (2009).
- Y.-C. K. Chen-Wiegart, R. DeMike, C. Erdonmez, K. Thornton, S. A. Barnett, and J. Wang, *Journal of Power Sources*, **249**, 349 (2014).
- L. Holzer, B. Iwanschitz, T. Hocker, B. Münch, M. Prestat, D. Wiedenmann, U. Vogt, P. Holtappels, J. Sfeir, A. Mai, and T. Graule, *Journal of Power Sources*, **196**, 1279 (2011).
- L. Moggi, F. Prado, and A. Caneiro, *Chemistry of Materials*, **18**, 4163 (2006).
- L. Moggi, F. Prado, C. Jimenez, and A. Caneiro, *Solid State Ionics*, **240**, 19 (2013).
- P. V. H. Martin Sogaard, Mogens Mogensen, and E. S. Finn Willy Poulsen, *Solid State Ionics*, **177**, 3285 (2006).
- L. Wang, R. Merkle, Y. A. Mastrikov, E. A. Kotomin, and J. Maier, *Journal of Materials Research*, **27**, 2000 (2012).